Using Image Quality Metrics to Optimize the Design of Integrated Medical Ultrasound ADCs

Radeljic-Jakic, Nikola; Flikweert, Adriaan J.; Rozsa, Nuriel N.M.; Vos, Hendrik J.; Pertijs, Michiel A.P.

DOI
10.1109/TUFFC.2025.3577258

Publication date
2025

Document Version
Final published version

Published in
IEEE Transactions on Ultrasonics, Ferroelectrics, and Frequency Control

Using Image Quality Metrics to Optimize the Design of Integrated Medical Ultrasound ADCs

Nikola Radeljic-Jakic, *Graduate Student Member, IEEE*, Adriaan J. Flikweert, *Member, IEEE*, Nuriel N. M. Rozsa, *Member, IEEE*, Hendrik J. Vos, *Member, IEEE*, and Michiel A. P. Pertijs, *Senior Member, IEEE*

***Abstract*—Emerging handheld and wearable ultrasound devices enable diagnosis and long-term monitoring outside clinical settings. They require a low-power, highly complex, locally integrated system to process the RF data. The analog-to-digital converter (ADC) is a critical building block in the receive chain of these systems as it enables digital beamforming and image reconstruction. However, the ADCs currently used in cart-based imaging systems are bulky and consume too much power to be integrated into battery-powered devices. This article investigates how the area and power consumption of the commonly used successive approximation register (SAR) ADC can be reduced without negatively affecting B-mode and color-Doppler image quality. A Monte Carlo (MC) simulation study was performed in which RF data acquired with a phased-array transducer in Field II were digitized using a model of a nonideal ADC. Five different nonidealities were applied to four commonly used SAR-ADC architectures. B-mode and color-Doppler images were reconstructed from the digitized RF data. The impact of the nonidealities on the image quality was evaluated by means of three image quality metrics (IQM): peak signal-to-noise ratio (PSNR), structural similarity index (SSIM), and contrast-to-noise ratio (CNR). The effectiveness of error correction and ways of calibration are also discussed. The results show that both B-mode imaging and color-Doppler imaging are inherently resilient to nonidealities, particularly capacitor mismatch, leading to relaxed ADC requirements and paving the way for more practical in-probe digitization.**

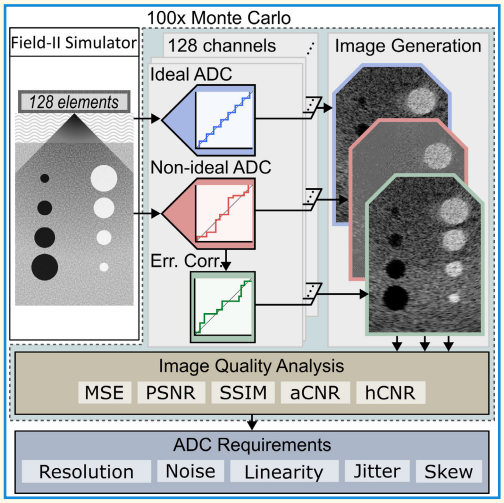

***Index Terms*—Application-specific integrated circuit (ASIC), error correction, image quality metrics (IQM), in-probe digitization, medical ultrasound, successive approximation register analog-to-digital converter (SAR-ADC).**

I. Introduction

ULTRASOUND imaging has become one of the most widely used clinical imaging modalities [1]. Compared with other imaging modalities, such as computed tomography and magnetic resonance imaging, ultrasound is relatively inexpensive and versatile [2]. Unlike positron emission tomography and X-ray, it does not expose the patient to ionizing radiation. Furthermore, ultrasound probes offer the unique ability of real-time noninvasive imaging. A downside of traditional ultrasound probes is that they require a relatively bulky and expensive cart-based imaging system and rely on a skilled operator to generate high-quality images. As a result, medical ultrasound imaging is currently restricted to clinical settings.

Several all-in-one probes have been introduced, incorporating most of the ultrasound system's functionality into the probe [3]. These handheld battery-powered solutions can be connected to a smartphone or tablet. In addition, a medical trend toward long-term monitoring has led to the development of compact wearable ultrasound devices [4]. These devices are usually attached to a fixed position on a patient's body with an adhesive for long-term monitoring without the need for an operator or the usual movement restrictions that apply during a clinical procedure [5], [6].

However, handheld and wearable devices require a highly complex, locally integrated system to process ultrasound data.

Received 4 April 2025; accepted 1 June 2025. Date of publication 6 June 2025; date of current version 28 July 2025. *(Corresponding author: Nikola Radeljic-Jakic.)*

Nikola Radeljic-Jakic is with Oldelft Ultrasound, 2629 JG Delft, The Netherlands, and also with the Electronic Instrumentation Laboratory, Delft University of Technology, 2628 CD Delft, The Netherlands (e-mail: nradeljic@oldelft.nl).

Adriaan J. Flikweert is with Oldelft Ultrasound, 2629 JG Delft, The Netherlands (e-mail: aflikweert@oldelft.nl).

Nuriel N. M. Rozsa and Michiel A. P. Pertijs are with the Electronic Instrumentation Laboratory, Delft University of Technology, 2628 CD Delft, The Netherlands (e-mail: n.n.m.rozsa@tudelft.nl; m.a.p.pertijs@tudelft.nl).

Hendrik J. Vos is with the Laboratory of Acoustical Wavefield Imaging, Delft University of Technology, 2628 CJ Delft, The Netherlands, and also with the Department of Biomedical Engineering, Thoraxcenter, Erasmus University Medical Center (Erasmus MC), 3015 CN Rotterdam, The Netherlands (e-mail: h.vos@erasmusmc.nl).

Digital Object Identifier 10.1109/TUFFC.2025.3577258

Highlights

- **To reduce the area and power of in-probe analog-to-digital converters (ADCs), we studied the impact of non-idealities of successive-approximation register (SAR) ADCs on ultrasound image quality.**
- **B-mode and color-Doppler imaging are inherently resilient to ADC non-idealities. Compared to general purpose SAR-ADCs, capacitor matching can be significantly relaxed without degrading image quality.**
- **The presented strategy can be used to design more area- and power-efficient ADCs for handheld and wearable ultrasound devices and other ultrasound devices using in-probe digitization.**

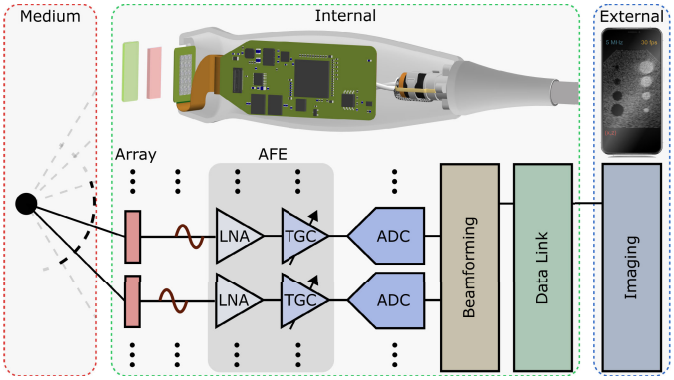

Fig. 1. Overview of the receive path of a locally integrated handheld ultrasound device.

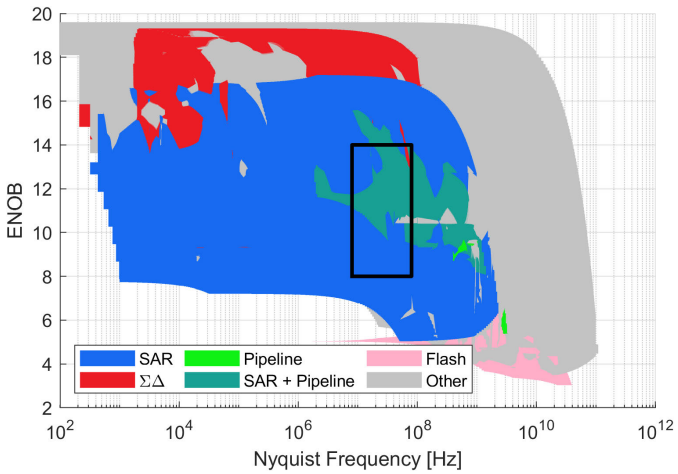

Fig. 2. Color plot displaying the top-performing ADC architectures in terms of power per conversion for combinations of Nyquist frequency and ENOB. The medical ultrasound ADC ROI is indicated with a black rectangle.

A typical handheld receive chain would look like in Fig. 1, consisting of analog frontends (AFEs) providing low-noise amplification (LNA) and time-gain compensation (TGC), analog-to-digital converter (ADC), a beamforming stage, a data link, and a smart device for final image reconstruction. These systems need to be compact and battery-powered to limit movement restrictions. Consequently, their power consumption needs to be low to enable long-term monitoring without the hassle of charging too often.

The ADC is a critical building block in the receive chain of medical ultrasound devices as it digitizes the analog ultrasound data for digital beamforming and image generation. However, it is nontrivial to integrate ADCs into battery-powered devices due to power consumption and area constraints.

Similar constraints exist for medical ultrasound probes and catheters. In those fields, application-specific integrated circuits (ASICs) containing ADCs are used to reduce the cable count without the downsides associated with purely analog techniques [7], [8], [9]. In the digital domain, where signals are more robust against sources of interference, they can be more easily combined with time-domain multiplexing (TDM) techniques, resulting in fewer channels. Combining in-probe digitization with analog techniques can lead to cable count reductions up to two orders of magnitude [10]. For applications such as intracardiac echocardiography, where catheters enter the bloodstream to acquire detailed anatomical information about the patient's heart, the devices are commonly restricted to single use to prevent complications [11]. They could greatly benefit from the cost reduction due to lower cable counts.

The power efficiency of the most commonly used ADC architectures is plotted as a function of the sampling frequency and the effective number of bits (ENOB) in Fig. 2 using data from [12]. The visible color indicates the most power-efficient architecture as a function of sampling frequency and ENOB. Considering a typical center frequency from 2 to 20 MHz for medical ultrasound imaging [13] and a fractional bandwidth of up to 100%, a region of interest (ROI) between 8 and 14 bits and a sampling frequency of 8 and 80 MHz have been marked in Fig. 2. We can see that the successive approximation register (SAR) ADC and SAR+Pipeline structures are the most power-efficient architectures in the ROI. Therefore, it comes as no surprise that the SAR-ADC architecture or a hybrid solution, including the SAR-ADC, is a common choice for ultrasound ADCs [14], [15], [16]. Nevertheless, these implementations consume significant amounts of the available power inside the probe, limiting battery life in handheld and wearable devices.

To investigate means of reducing ADC power consumption, it is helpful to study the impact of ADC nonidealities on ultrasound image quality. Ultrasound images are conventionally reconstructed by applying beamforming techniques such as delay-and-sum (DAS) to the electric signals from the transducer elements. Such techniques coherently sum RF data and thus reduce the effect that noncoherent data, as induced by some of the ADC nonidealities, have on the image. For example, the impact of bit errors on the ultrasound image quality was found to be limited in [17].

We study the impact of ADC nonidealities on postprocessed images—not on the electrical signal—to achieve better trade-offs between performance and cost. In this work, we focus on the design of a 12-bit ADC with a sampling frequency of 20 MHz. A simulation model was developed to assess

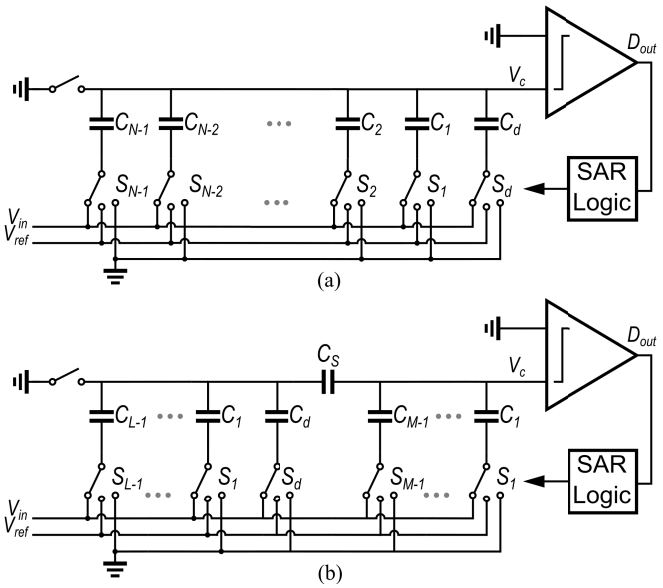

Fig. 3. Schematic of a charge-redistribution SAR-ADC with (a) normal CDAC and (b) split CDAC.

ultrasound image quality in the presence of SAR-ADC nonidealities and related error corrections using image quality metrics (IQMs). We compared how different nonidealities affect B-mode and color-Doppler image quality for various SAR-ADC architectures. The simulation results show that ultrasound image quality is weakly affected by capacitor mismatch. Compact ADC architectures that would be unacceptable in terms of performance of general-purpose ADCs can be used for ultrasound imaging, leading to a factor of 32 reduction in area and switching power for the targeted ADC. Therefore, smaller and more power-efficient architectures can be used if ADC requirements are derived from the image quality.

Section II gives an overview of SAR-ADC nonidealities and their effects on the electrical signal, followed by a description of the simulation setup used to evaluate their effects on the image quality in Section III. Next, the results are shown and discussed in Sections IV and V, respectively. Finally, the main findings are summarized in Section VI.

II. Theory

In this section, we first explain the operating principle of the conventional SAR-ADC and compare it with the more compact split-CDAC architecture. We then discuss how different nonidealities affect the performance of the ADC.

A. SAR-ADC Operating Principles

A conventional charge-redistribution SAR-ADC [18] as shown in Fig. 3(a) consists of a comparator, SAR logic, switches, and an N-bit capacitive digital-to-analog converter (CDAC). The value of each capacitor in the CDAC is defined by

$$C_n = 2^{n-1} \cdot C_u \tag{1}$$

where n indicates the nth capacitor, and C_u is the unit capacitance of the CDAC. A dummy capacitor C_d with a size of C_u is placed in parallel to the CDAC, bringing the total capacitance to $2^N \cdot C_u$, to prevent gain errors.

A conventional charge-redistribution SAR-ADC operates in three phases. In the sampling phase, the top plate of the CDAC is grounded, and the bottom plate is connected to the input signal V_{in}, resulting in a total charge on the bottom plate of the CDAC of

$$Q_{\text{in}} = C_{\text{tot}} \cdot V_{\text{in}}. \tag{2}$$

During the hold phase, the bottom plate is connected to ground, while the top plate is disconnected from ground, resulting in a comparator input voltage of

$$V_c = -V_{\text{in}}. \tag{3}$$

In the redistribution phase, the conversion is performed recursively by charge redistribution. During the first conversion step, the largest capacitor (C_{N-1}) is connected to the reference voltage through switch S_{N-1}, forming a 1:1 capacitive divider with the remaining capacitors, which are still connected to ground. The comparator input voltage becomes

$$V_c = -V_{\text{in}} + \frac{V_{\text{ref}}}{2}. \tag{4}$$

The comparator determines the sign of V_c. If the output is negative, the most significant bit (MSB) is set to "1," and C_{N-1} remains connected to V_{ref}. However, if the output is positive, the MSB is set to "0," and C_{N-1} is connected to ground. This procedure is repeated until all the bits have been resolved.

The split-capacitor CDAC SAR-ADC [19] shown in Fig. 3(b) is often used to reduce the size of the CDAC. It divides the N-bit capacitor array into M MSBs and $L = N - M$ least significant bits (LSBs). The coupling capacitor C_s scales the output of the LSBs by a factor of 2^L and its value is defined by

$$C_s = \frac{2^L}{2^L - 1} \cdot C_u. \tag{5}$$

In addition, the total value of the MSB capacitors is also reduced by a factor of 2^L, resulting in area and power savings. Conversely, the smaller capacitance results in a higher random mismatch between the capacitors [20].

B. Quantization Error

The quantization error is a systematic error introduced by the finite resolution of any ADC when an analog signal is digitized. For ADCs with a resolution of 7 bits or higher, the quantization error can be approximated as white noise between 0 and $f_s/2$ [19]. The quantization error spectrum was first analyzed in [21]. After simplifications, the root-mean-square (rms) quantization noise voltage can be expressed as

$$v_{q,\text{rms}} = \frac{v_q}{\sqrt{12}} \tag{6}$$

where v_q is the quantization step, which is the input change that corresponds to an ideal LSB step in the ADC's output code. The v_q of a N-bit ADC can be expressed as

$$v_q = \frac{V_{\text{FSR}}}{2^N} \tag{7}$$

where V_{FSR} is the full-scale analog input range of the ADC, typically equal to the reference voltage V_{ref}. The maximum achievable signal-to-quantization-noise ratio SNR_q in dB [often referred to as signal-to-quantization-noise ratio (SQNR)] for a full-scale sinusoidal input can be calculated by

$$\mathrm{SNR}_q = 1.76 + N \times 6.02. \tag{8}$$

For example, a 12-bit ADC's SNR_q is maximally 74 dB.

C. Thermal Noise

The dominant thermal noise sources in SAR ADCs are typically the rms kT/C noise [22] due to sampling and the comparator noise. The $1/f$ (flicker) noise [22] can be neglected since the band of interest is above the $1/f$ corner frequency. The kT/C noise due to sampling is given by

$$v_{n,s} = \sqrt{\frac{kT}{C_{\mathrm{DAC}}}} \tag{9}$$

where k is Boltzmann's constant, T is the absolute temperature, and C_{DAC} represents the total CDAC capacitance.

Assuming the comparator's noise is dominated by the input differential pair with transconductance g_m, the rms input-referred comparator noise can be expressed as

$$v_{n,\mathrm{cmp}} = \sqrt{\frac{8kT\gamma \cdot \mathrm{BW}}{g_m}} \tag{10}$$

where BW is the bandwidth of interest and γ is a coefficient that depends on the device characteristics [22].

The total resulting SNR due to thermal noise for a full-scale sinusoidal input, expressed in dB, is

$$\mathrm{SNR}_{\mathrm{th}} = 20 \cdot \log_{10}\left(\frac{V_{\mathrm{FSR}}/\sqrt{2}}{\sqrt{v_{n,s}^2 + v_{n,\mathrm{cmp}}^2}}\right) \tag{11}$$

and is typically chosen 3 dB higher than the targeted SQNR.

D. Capacitor Mismatch

The integral nonlinearity (INL) is a commonly used performance metric that describes the deviation of the measured threshold levels of an ADC with respect to its ideal threshold levels [19]. The INL is usually reported as a single value representing the maximum INL across all the transitions. In SAR ADCs, the INL is typically determined by the capacitor mismatch. Capacitor mismatch, the deviation of capacitor values from the specified ideal value, can be divided into random and systematic capacitor mismatch, leading to nonlinear transfer characteristics. Process variations cause random mismatch, whereas layout irregularities typically induce systematic mismatch. Random capacitor mismatch can be described by

$$\frac{\sigma_{\Delta C}}{C} = \frac{A_C}{\sqrt{C}} \tag{12}$$

where $\sigma_{\Delta C}$ is the standard deviation of the difference between equally designed capacitors, C is their nominal value, and A_C is a constant for a given IC technology expressed in $\%(\mathrm{fF})^{1/2}$ [19]. This shows that matching can be improved by increasing the capacitor size. Capacitor matching becomes especially important for higher ADC resolutions, where the smaller quantization steps lead to increased matching requirements. For high-resolution ADCs, this leads to larger unit capacitor sizes, larger areas, and reduced power efficiency.

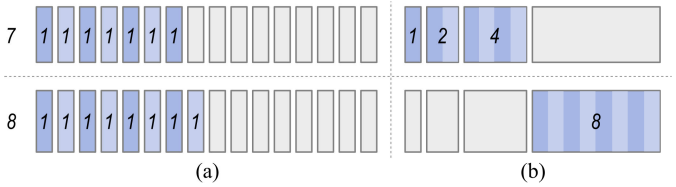

Fig. 4. (a) Unary and (b) binary representations for digital-to-analog conversion of codes 7 and 8.

The unary and binary representations shown in Fig. 4 are the two most commonly used capacitor configurations in SAR ADCs [19]. The unary representation uses a series of identically scaled capacitors, whereas the binary representation uses a series of exponentially growing capacitors built out of multiple unit capacitors. The number of switches required to control all the capacitors in the unary representation is 2^N, whereas it is only N for the binary representation. This means that binary representations can be designed with a lower area and switching power consumption.

However, problems with linearity limit the use of the binary representation for ADCs with resolutions higher than 10–12 bits. The unary representation is inherently monotonous because the capacitance always increases for higher values, whereas that is not guaranteed for the binary representation. In the example of Fig. 4(b), it could happen that due to capacitor mismatch, the total capacitance defining output code 7 is higher than the total capacitance defining output code 8, resulting in nonmonotonous transfer characteristics for certain ADC topologies [19]. For SAR ADCs, however, the transfer always remains monotonous because the bits are evaluated from most significant to least significant, limiting the effect of capacitor mismatch to unequal quantization steps.

The maximum INL is generally designed to be lower than 0.5 LSB to have a negligible effect on the sampled signal. For example, to reach this INL requirement for a 12-bit ADC, the maximum capacitor mismatch coefficient for the unary representation is given by [19]

$$\frac{\sigma_{\Delta C}}{C} \cong \frac{\sigma_{\mathrm{INL}}}{\sqrt{2^{N-2}}} = 1.56\%. \tag{13}$$

E. Clock Skew

In large sensor-array systems such as ultrasound imagers, the clock signal arrives at the on-chip ADCs at different times due to differences in routing or digital circuit design. This translates to different but fixed levels of clock delay for each ADC, resulting in unwanted time differences between their sampled RF data.

F. Clock Jitter

Clock jitter, unlike clock skew, is a random deviation from the ideal sampling moment. A jitter Δt results in an error

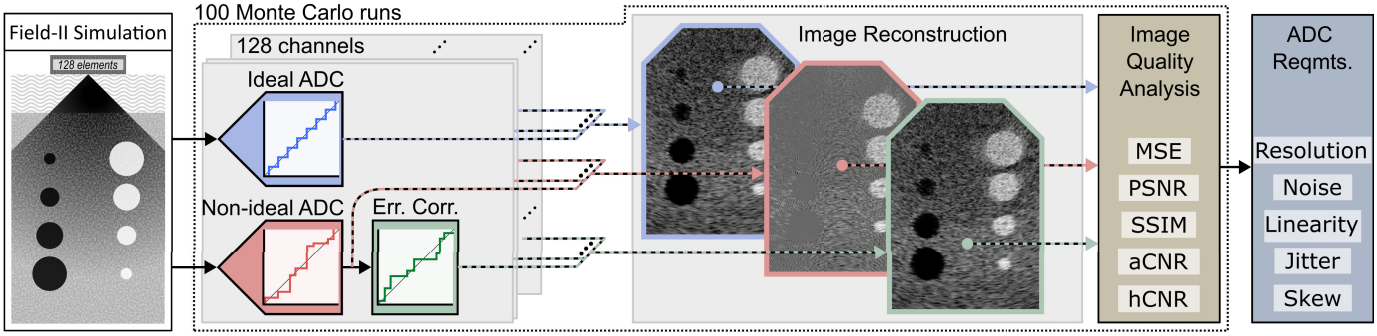

Fig. 5. Block diagram of the MATLAB simulation architecture.

voltage of

$$v_{\text{err,jit}} = \Delta t \frac{dV_{\text{in}}}{dt}. \tag{14}$$

The worst case error occurs at the zero-crossings of a full-scale sinusoidal signal. To reach a noise specification of half an LSB, the maximum value for the jitter can be calculated by

$$\Delta t < \frac{1}{2\pi f_{\text{in}} 2^N}. \tag{15}$$

For example, for a 12-bit 20 MS/s ADC with a bandwidth of 10 MHz, the maximum allowed jitter is <4 ps (80 ppm).

TABLE I
PHASED-ARRAY SIMULATION PARAMETERS

Parameter	Value	Unit
Aperture (x × y)	19.7 × 5.0	mm^2
No. of elements	128	—
Center frequency (f_c)	5	MHz
Wavelength (λ)	308	μm
Pitch	0.50	λ
Kerf	0.05	λ
Element width (x)	0.45	λ
Element length (y)	5	mm

III. METHODS

A. Overview

A MATLAB model of an ultrasound probe with digitization was used to evaluate the effects of SAR-ADC nonidealities on ultrasound image quality. The simulation flow is illustrated in Fig. 5. Raw RF element data were simulated from cyst, vessel, and fetus phantoms with a predefined transducer array using the Field-II program in MATLAB [23], [24] with a sampling rate of 20 MHz. The cyst and vessel phantoms were used to evaluate the B-mode and color-Doppler image quality, respectively. The RF data were digitized by an ideal ADC and a nonideal ADC where nonidealities were introduced. In addition, the output of the nonideal ADC was corrected for INL due to capacitor mismatch. Images were reconstructed from the output data of the ideal ADC, the output of the nonideal ADC before error correction, and the output of the nonideal ADC after error correction. Finally, the IQM were calculated, and ADC requirements were derived.

B. Raw Echo Data Acquisition

Simulations were performed for a 128-element phased-array transducer in the Field-II program in MATLAB. The transducer details are shown in Table I.

All the elements were active for each pulse-echo simulation; steering focused beams from −45° to +45° with a 0.91° angular step, resulting in a total of 100 scanlines. A fixed transmit focal point was placed at 50 mm, whereas dynamic focusing was applied to the received echoes. The elements were excited by a two-period sinusoidal pulse, and Hanning apodization was applied both in transmit and receive. Propagation attenuation was not considered since we assume it would be compensated for by TGC in the AFE. Instead of setting a noise floor in Field-II, the noise was added to the generated raw RF element data to be evaluated separately.

Three simulation phantoms (based on the examples in [23], [24], [25]) were used to evaluate the B-mode and color-Doppler imaging modalities. The cyst phantom shown in Fig. 6(a) has a size of 40 × 10 × 55 mm (x, y, z) and is positioned 10 mm from the surface of the transducer. This phantom comprises roughly 140 000 scatterers, and the region between the transducer and phantom is acoustically transparent. Four anechoic regions were placed at different depths in the phantom at a −10-mm offset from the array's center, whereas four hyperechoic regions were placed at a +10-mm offset. The scatterer amplitudes were set to 0 and 10 for the anechoic and hyperechoic regions, respectively. The amplitudes of the background scatterers follow a Gaussian distribution with a μ of 0 and a σ of 1, where a negative value of the scattering amplitude represents a phase shift of π in the received echo.

The vessel phantom shown in Fig. 6(b) has a size of 40 × 10 × 60 mm (x, y, z) and is positioned 10 mm from the surface of the transducer. The static part of the phantom is composed of roughly 140 000 scatterers, and the region between the transducer and phantom is acoustically transparent. The vessel comprises roughly 35 000 scatterers representing the blood in the vessel, has a diameter of 10 mm, and is rotated 45° from the surface of the transducer. The amplitudes of the background scatterers follow a Gaussian distribution with a μ of 0 and a σ of 1. The amplitude of the blood scatterers inside the vessel is reduced by 40 dB with respect to the background scatterers [26]. The flow profile is parabolic with a maximum velocity of 1 m/s in the vessel's

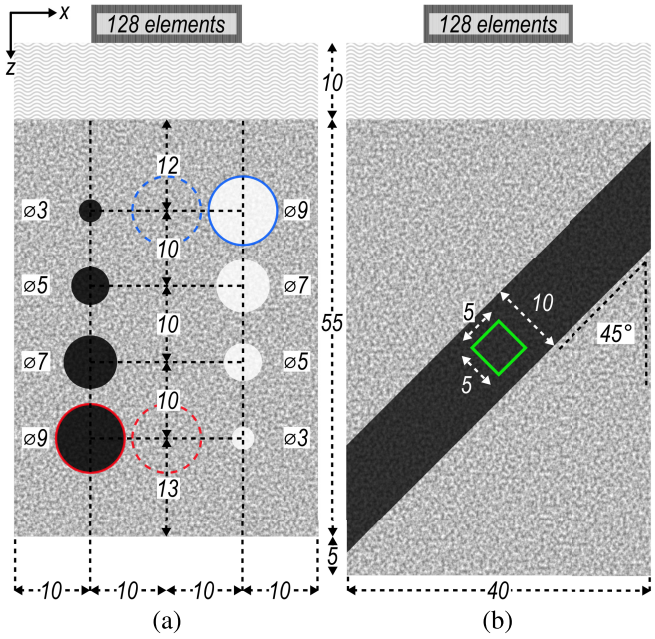

Fig. 6. Field-II simulation setup with a 128-element phased-array transducer with (a) cyst-phantom for B-mode imaging and (b) a vessel phantom for color-Doppler imaging. All the dimensions are given in mm. The red- and blue-colored circles indicate the regions used for CNR calculations, and the green diamond area indicates the area used for flow velocity calculations.

center. To calculate the flow, ten consecutive acquisitions are taken with a pulse repetition frequency (PRF) of 10 kHz.

A complex fetus phantom containing sharp transitions between anechoic and hyperechoic regions was used to highlight potential artifacts not seen in the cyst phantom. The phantom has a size of $80 \times 15 \times 60$ mm (x, y, z) and is positioned 20 mm from the surface of the transducer. It comprises roughly 200 000 scatterers, and the region between the transducer and phantom is acoustically transparent.

C. ADC Modeling

An ADC model was designed in MATLAB that quantized the RF data, where each transducer is connected to a unique ADC. The RF data were scaled such that the highest reflected pulses are equal to the full-scale input range of the ADC (-0.4 to 0.4 V). The ADCs were modeled as SAR-ADCs with a configurable ADC architecture, resolution, DAC switching scheme, and nonidealities. The conventional and split-CDAC architectures were simulated with the unary and binary switching schemes.

The nonidealities were introduced individually per ADC with uncorrelated Gaussian distributions. The noise was introduced at the comparator input. Nonlinearity was introduced in the CDAC through random deviations in capacitor values, representing the capacitor mismatch. The unit capacitance was constant over all the simulations. The clock skew was a preset random value per ADC, resulting in constant time delays between transducer elements. The clock jitter values were used to interpolate between samples of the RF data, resulting in random time delays between samples.

D. Calibration and Correction

The ADC was calibrated by applying a ramp input over the entire input range and recording the transfer curve. The INL of all the digital output codes was stored in a lookup table (LUT). The LUT was used to correct the signal values by subtracting the INL from the quantized output signals. This reduced the nonlinearity caused by capacitor mismatch, after which a corrected image was reconstructed.

E. Image Reconstruction

Images were reconstructed from ideal ADC output data, uncorrected nonideal ADC output data, and corrected nonideal ADC output data by means of DAS beamforming with dynamic receive focusing. The beamformed signals at location (x, z) are expressed by

$$S(x, z) = \sum_{e=1}^{E} w_e(x, z) \cdot y_e(x, z) \tag{16}$$

where e represents the element number, E represents the total number of elements, $w_e(x, z)$ represents the apodization weight of the Tukey window applied to the signal of element e, and $y_e(x, z)$ represents the delayed element response of element e. To reduce the errors introduced by the finite sampling rate, linear interpolation between samples was used to attain a more accurate value of $y_e(x, z)$. The envelope of the signal is extracted by performing a Hilbert transformation.

For the B-mode image, the absolute value of the envelope is normalized and converted into the log domain, after which it is displayed as a 50-dB greyscale image [27]. All the signal intensities below -50 dB are set to -50 dB. The image's pixel values were scaled between 0 and 255 and stored in double-precision format for further image quality analysis.

For the color-Doppler image, autocorrelation was used to estimate the mean velocity of the blood flow from ten consecutive B-mode acquisitions [28]. To prevent blooming [29], the optimal color-gain settings were acquired by running a global optimization algorithm set to obtain the highest structural similarity index (SSIM). For this algorithm, we assumed that no local minima existed. The image's pixel velocities in m/s were stored in double-precision format for further image quality analysis.

F. Image Quality Analysis

First, the ideal ADC output data were used to reconstruct an error-free reference image. The erroneous data resulting from the introduction of nonidealities were then used to reconstruct the degraded images. Three full-reference IQMs were used to get an objective measure of the B-mode image quality degradation in the presence of these nonidealities: the peak signal-to-noise ratio (PSNR) [30], the SSIM [31], and the anechoic and hyperechoic contrast-to-noise ratio (CNR) [32]. The color-Doppler image quality was evaluated using the SSIM IQM, and the accuracy of the velocity was evaluated by calculating the root-mean-square error (RMSE) in the area marked with green in Fig. 6.

The PSNR is an expression for the ratio of the peak pixel power of the reference image and the mean-squared error

(mse) of the degraded image when compared with the reference image [30]. PSNR is usually expressed in dB because of the wide dynamic range (DR) of the evaluated signals [30]

$$\text{PSNR} = 10 \cdot \log_{10}\left(\frac{I^2}{\text{mse}}\right) \tag{17}$$

where I is the maximum possible pixel value, equal to 255 for an 8-bit B-mode image. The mse is specified by [30]

$$\text{mse} = \frac{1}{r \cdot c}\sum_{i=1}^{m}\sum_{j=1}^{n}\left[R(i,j) - D(i,j)\right]^2 \tag{18}$$

in which r and c represent the number of rows and columns in the image, respectively, and R and D are valued between 0 and 255, representing the pixel values in the reference and distorted images, respectively. The PSNR metric is simple but correlates poorly with perceived image quality.

The SSIM is based on human perception and correlates more with perceived image quality. While other IQMs, such as PSNR and mse, estimate the absolute errors, the SSIM uses the structural information present in the image, together with a luminance and contrast term, in a single IQM [31]. Structural information refers to the theory that the pixels have strong local spatial dependencies. The mean intensity determines the luminance term, and the standard deviations determine the contrast. The SSIM is expressed by [31]

$$\text{SSIM} = \frac{(2\mu_R\mu_D + C_1)(2\sigma_{RD} + C_2)}{(\mu_R^2 + \mu_D^2 + C_1)(\sigma_R^2 + \sigma_D^2 + C_2)} \tag{19}$$

where μ_R and μ_D are the mean, σ_R and σ_D are the standard deviation, and σ_{RD} is the cross-covariance of the two images. C_1 and C_2 are specified by $C_n = (K_n L)^2$, where $K_1 = 0.01$, $K_2 = 0.03$ as in [31], and L is the DR of the image which is set to 255.

As the name suggests, the CNR measures an image's contrast. It is a valuable measure for quantifying the detectability of cysts from the background and is given by [33]

$$\text{CNR} = \frac{|\mu_{\text{ROI}} - \mu_{\text{BG}}|}{\sqrt{\sigma_{\text{ROI}}^2 + \sigma_{\text{BG}}^2}} \tag{20}$$

where μ_{ROI} and μ_{BG} represent the mean values inside and outside an ROI, respectively, and σ_{ROI} and σ_{BG} are the respective standard deviations. The 9-mm anechoic and hyperechoic ROIs used to calculate the anechoic CNR (aCNR) and hyperechoic CNR (hCNR) are encircled in red and blue, respectively (Fig. 6). The corresponding background regions are indicated with dashed circles of the same color.

IV. Results

The B-mode and color-Doppler reference images shown in Fig. 7 were reconstructed from the ideal ADCs output data. In Section IV-A, we determine the robustness of the different SAR-ADC architectures against mismatch. Subsequently, we use the most robust architecture to evaluate the effect of the other ADC nonidealities in Sections IV-B–IV-D.

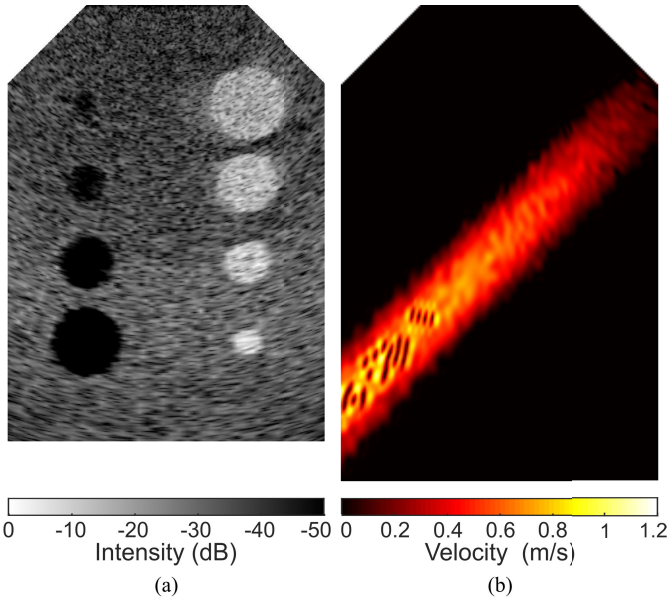

Fig. 7. (a) B-mode and (b) color-Doppler reference images reconstructed from the RF data.

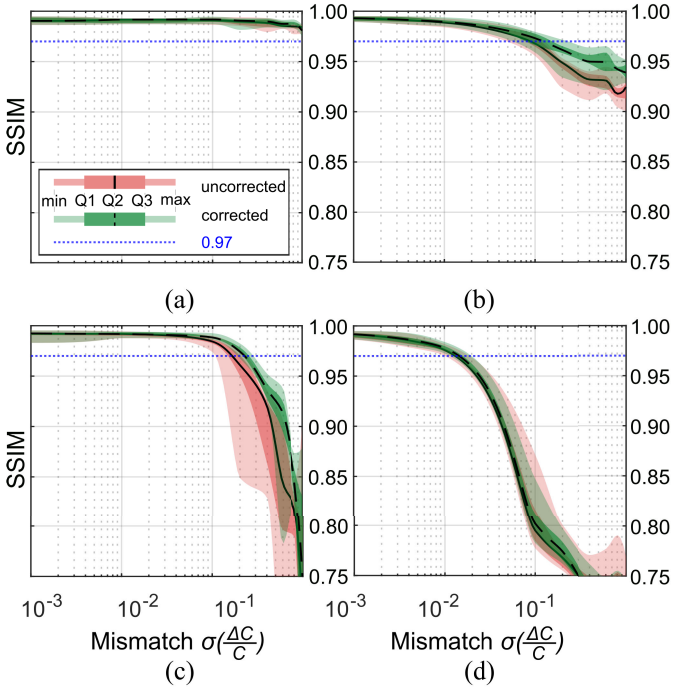

Fig. 8. Interpolated box plot generated from ten MC runs, displaying the SSIM of the color-Doppler images for (a) conventional-unary, (b) conventional-binary, (c) split-unary, and (d) split-binary architectures. The min and max represent the smallest and largest numbers in the dataset, respectively. Q1, Q2, and Q3 are the dataset's first, second, and third quartiles, respectively.

A. SAR-ADC Architecture Comparison

The effect of capacitor mismatch on color-Doppler image quality was simulated for multiple combinations of 12-bit CDAC structures and switching schemes using the SSIM IQM. The color-Doppler imaging mode was selected to evaluate the architectures as it is more sensitive to nonidealities than B-mode. Fig. 8 shows that the image quality remains high (SSIM $>$ 0.97) for the conventional-unary architecture for $\sigma(\Delta C)/C > 1$ before and after correction. The image

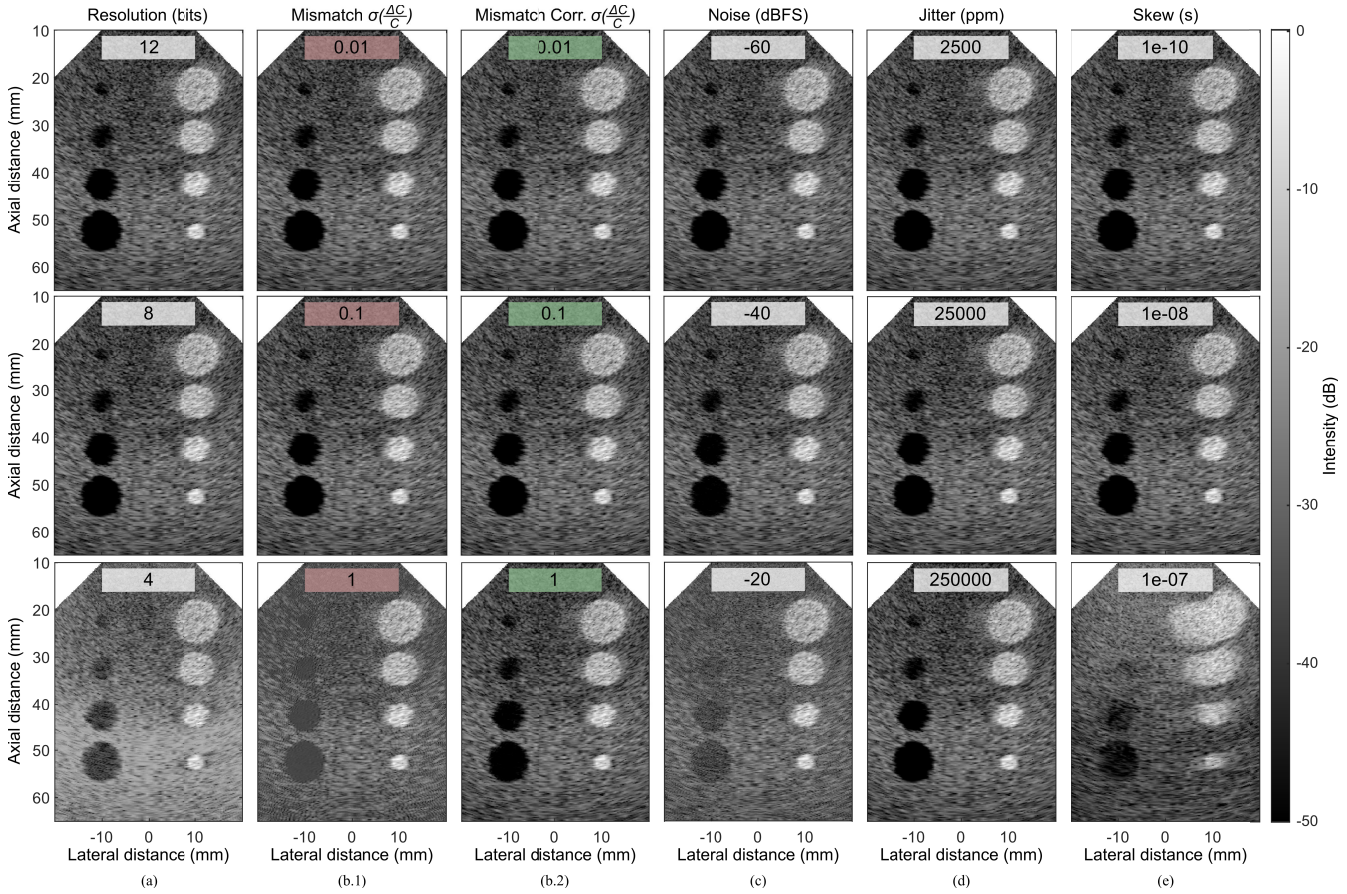

Fig. 9. Reference and distorted B-mode of a cyst phantom simulated with the phased-array transducer at different (a) resolution, (b.1) mismatch, (b.2) corrected mismatch, (c) noise, (d) jitter, and (e) skew levels. (b)–(e) Results for a 12-bit split-unary-CDAC SAR-ADC.

quality for the conventional-binary architecture remains high for $\sigma(\Delta C)/C \approx 0.09$ before correction and $\sigma(\Delta C)/C \approx 0.12$ after correction. The split-unary architecture retains a high image quality for $\sigma(\Delta C)/C \approx 0.16$ before correction and $\sigma(\Delta C)/C \approx 0.23$ after correction. The split-binary architecture performs significantly worse, as the SSIM decreases from $\sigma(\Delta C)/C \approx 0.01$. A higher standard deviation can be observed for the split architectures, as the color-Doppler imaging quality is strongly related to the location of the introduced nonlinearities. We use the split-unary CDAC architecture for the remaining simulations as it is the most compact architecture with realistically achievable matching specifications for ASICs.

B. B-Mode

We used the PSNR, SSIM, aCNR, and hCNR IQMs to analyze the B-mode image quality.

1) Quantization Error: Fig. 9(a) shows a subset of the reconstructed images for different ADC resolutions. We can observe that the hyperechoic regions are minimally affected by ADC resolution. In contrast, the anechoic and background regions experience increased noise, visible loss in boundary sharpness, and loss of contrast for ADC resolutions lower than 8 bits due to increasing quantization errors. While the PSNR increases for higher ADC resolutions, the SSIM, aCNR, and hCNR remain constant after $N \geq 8$, indicating that a resolution down to 8 bits can be tolerated without significant degradation of the image quality [Fig. 10(a)]. For the following nonidealities, the resolution of the ADC was set to 8 and 12 bits.

2) Mismatch: The capacitor mismatch $\sigma(\Delta C)/C$ was swept from 0 to 1. A subset of reconstructed images is shown in Fig. 9(b.1). The image quality experiences an increase in noise and loss of contrast for $\sigma(\Delta C)/C > 0.12$ for the 12-bit ADC. This is confirmed by the IQMs in Fig. 10(b). The boundary sharpness is largely unaffected by the mismatch. After correction, the overall effect of mismatch on the image is reduced significantly ($\sigma(\Delta C)/C > 0.59$) as can be seen in Figs. 9(b.2) and 10(b). The maximum allowed mismatch for the 8-bit ADC is 0.05 and 0.15, and for the uncorrected and corrected mismatch, respectively. Unsurprisingly, this is approximately a factor of 4 and can be explained by the 16-fold reduction in capacitors, resulting in a four times higher standard deviation.

In Fig. 10(b), we can see that the PSNR drops to 40 dB for $\sigma(\Delta C)/C > 0.21$, which can be seen as a unit capacitor standard deviation of 21%. After correction, the -3-dB drop in PSNR occurs at $\sigma(\Delta C)/C = 0.60$. However, the PSNR does not correlate well with perceived image quality, as the corrected image for a mismatch of $\sigma(\Delta C)/C = 1$ is almost indistinguishable from the ideal image. The SSIM and aCNR metrics match better with human perception for this phantom.

3) Noise: The ADC input noise was swept from -120 to 0 dBFS, and a subset of the reconstructed images is shown in Fig. 9(c). A visual increase in noise and loss of contrast

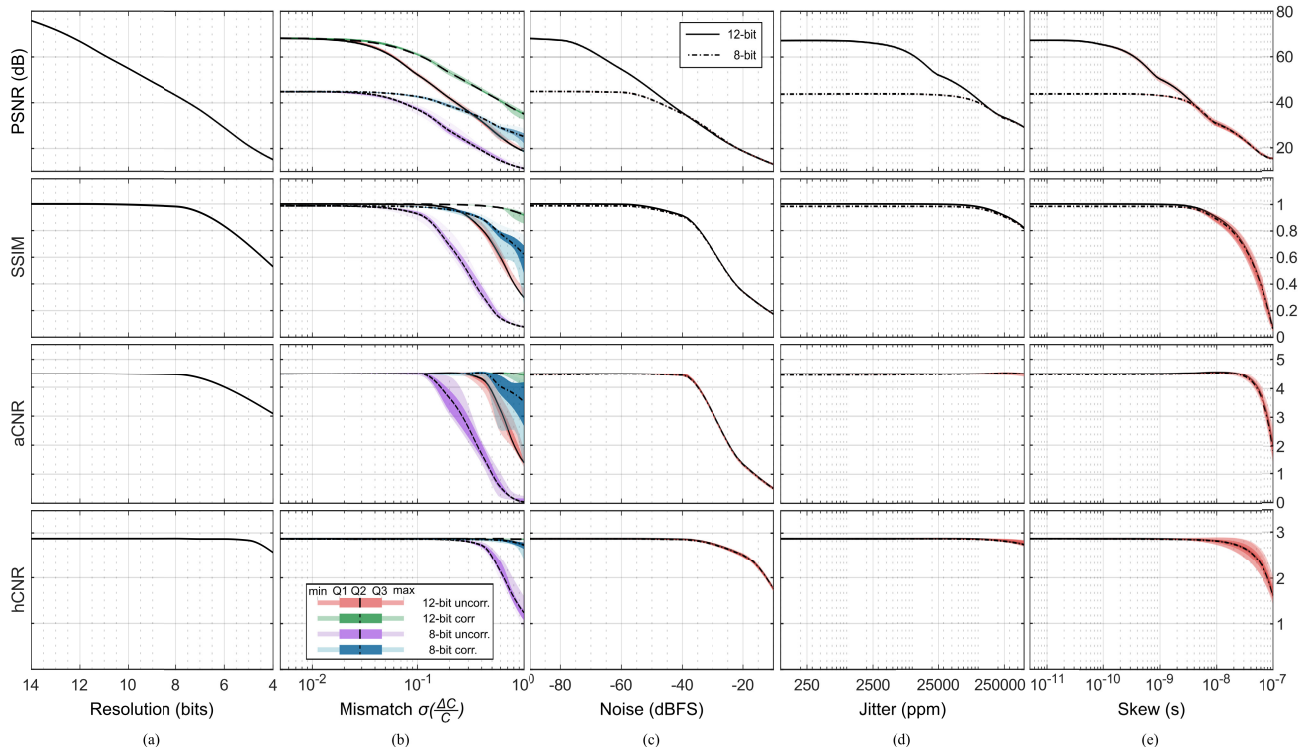

Fig. 10. Interpolated box plot generated from 100 MC runs, displaying the IQMs of the B-mode images of the fetus phantom versus (a) resolution, (b) mismatch, (c) noise, (d) jitter, and (e) skew levels for a 12-bit split-unary-CDAC SAR-ADC and an 8-bit split-unary-CDAC SAR-ADC. The min and max represent the smallest and largest numbers in the dataset, respectively. Q1, Q2, and Q3 are the dataset's first, second, and third quartiles, respectively.

can be observed for input noise levels higher than −40 dBFS. In Fig. 9(c), a −3-dB drop in PSNR is observed at a noise input level of −74 dBFS, equal to the single-channel 12-bit ADC SNR_q of 74 dB calculated using (8). Apart from the PSNR, the other IQMs are similar between the 8- and 12-bit ADCs.

4) Jitter: The ADC clock jitter was swept from 0.025 to 250 000 ppm with respect to a sampling period of 50 ns. Even for highest jitter values, no visual degradation of the image quality can be observed in Fig. 9(d), which the IQMs also confirm in Fig. 9(d). This is due to the averaging effect in DAS image reconstruction, which reduces the contribution of noncoherent signals. Apart from the PSNR, the other IQMs are similar between the 8- and 12-bit ADCs.

5) Skew: The ADC clock skew was swept from 1 to 100 ns, and a subset of reconstructed images is shown in Fig. 9(e). For $t_{\text{skew}} > 10$ ns, the lateral blurring increases due to interchannel timing mismatch. Apart from the PSNR, the other IQMs are similar between the 8- and 12-bit ADCs.

C. Color-Doppler

1) Quantization Error: The ADC resolution was swept from 4 to 14, and a collection of the reconstructed images is shown in Fig. 11(a). At a 10-bit resolution, some flow details are lost in the bottom left of the vessel. We also observe a loss of information at the vessel's edges for lower ADC resolutions. This information loss results from increased quantization noise levels, making it difficult to extract small blood flow signals without performing additional averaging steps. For resolutions lower than 8 bits, almost all the amplitude information of the blood flow is lost, and only the sign information of received signals remains. Nevertheless, a part of the flow can still be reconstructed due to the phase shift between consecutive captures. The SSIM and RMSE deteriorate at similar values.

2) Mismatch: The capacitor mismatch $\sigma(\Delta C)/C$ was swept from 0 to 1. A subset of the reconstructed images is shown in Fig. 11(b.1). The SSIM starts decreasing and the RMSE starts increasing for $\sigma(\Delta C)/C > 0.1$, where some artifacts can be seen at the edges of the vessel, and in the top right corner of the image, where the flow is nearly perpendicular to the steering angle. In contrast to B-mode imaging, the effectiveness of correction on the mismatch is limited, as can be seen in Figs. 11(b.2) and 12(b). This is due to the 40-dB reduction in amplitude for the blood scatterers with respect to the background scatterers used in the cyst phantom, resulting in small input signals at the ADC input. This means that only a small part of the ADC input range digitizes these signals, effectively reducing the ADC resolution for color-Doppler imaging. Furthermore, large nonlinearities can lead to broader or narrower quantization steps. If these large nonlinearities occur around zero, the SSIM will be lower than if they appear elsewhere, explaining the increased standard deviation in Fig. 12(b).

3) Noise: The ADC input noise was swept from −140 to 0 dBFS, and a subset of the reconstructed images is shown in Fig. 11(c). Some artifacts can already be observed at a noise input of −100 dBFS, and the SSIM remains relatively constant until −80 dBFS. However, for a noise level higher

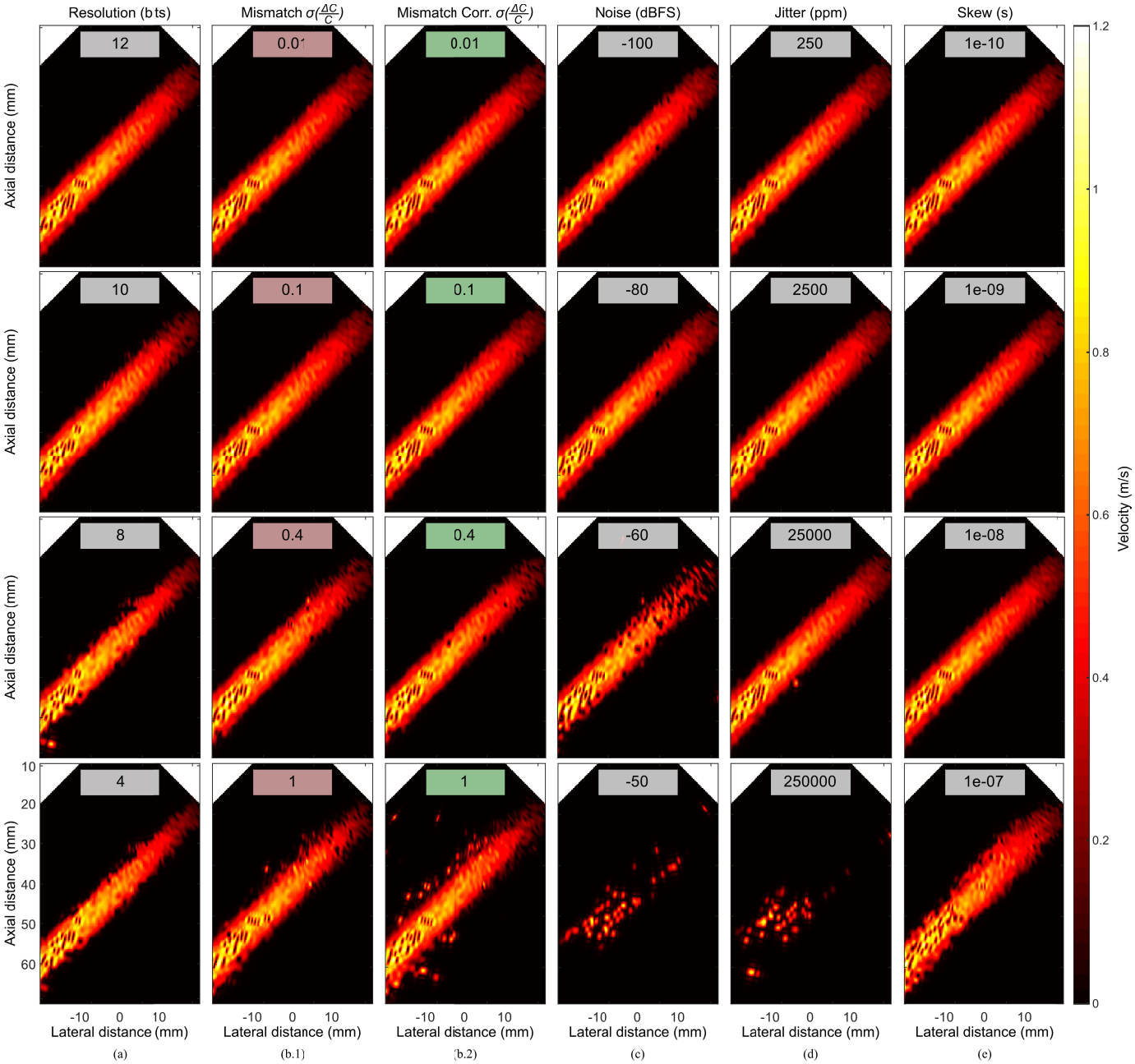

Fig. 11. Reference and distorted color-Doppler images for the phased-array transducer at different (a) resolution, (b.1) mismatch, (b.2) corrected mismatch, (c) noise, (d) jitter, and (e) skew levels. (b)–(e) Results for a 12-bit split-unary-CDAC SAR-ADC.

than −80 dBFS, the SSIM decreases and the RMSE increases, as can be seen in Fig. 12(c), at which point it is no longer possible to extract a high-quality color Doppler image.

4) Jitter: The ADC clock jitter was swept from 0.025 to 250 000 ppm [Fig. 12(d)]. For a jitter value of 250 000 ppm, the flow in the vessel starts to disappear within the vessel, and some artifacts appear at the edges of the vessel [Fig. 11(d)]. These artifacts are caused by windowing, resulting in nonzero values at the vessel's edges.

5) Skew: The ADC clock skew was swept from 1 to 100 ns [Figs. 11(e) and 12(e)]. For skew values larger than 10 ns, the image quality starts deteriorating as is confirmed by both the SSIM and RMSE.

D. B-Mode of Fetus Phantom

Fig. 13 shows the reference image (a) and reconstructed images at $\sigma(\Delta C)/C = 1$ before correction (b) and after correction (c). Similar to the cyst phantom, the images before correction experience an increase in noise and loss of contrast, while the boundary sharpness remains largely unaffected. After correction, the effect of mismatch on the image is reduced significantly, as seen in Fig. 14(b). Compared with the cyst-phantom, the resolution and noise requirements are increased by 1 bit and 10 dB, respectively. The mismatch, jitter, and skew requirements did not change significantly, as seen in Table II.

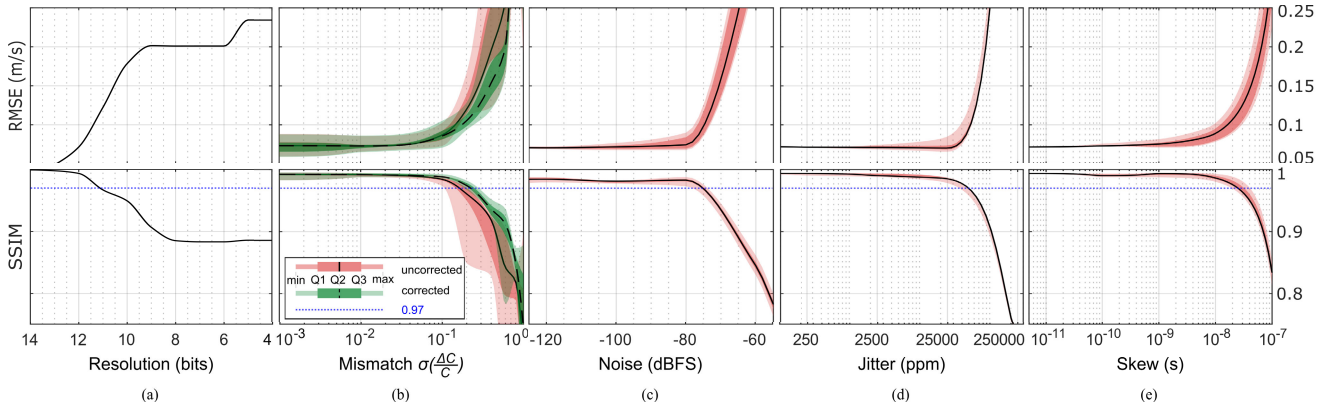

Fig. 12. Interpolated box plot generated from ten MC runs, displaying the RMSE and SSIM of the color-Doppler images versus (a) resolution, (b) mismatch, (c) noise, (d) jitter, and (e) skew levels. (b)–(e) Results for a 12-bit split-unary-CDAC SAR-ADC. The min and max represent the smallest and largest numbers in the dataset, respectively. Q1, Q2, and Q3 are the dataset's first, second, and third quartiles, respectively.

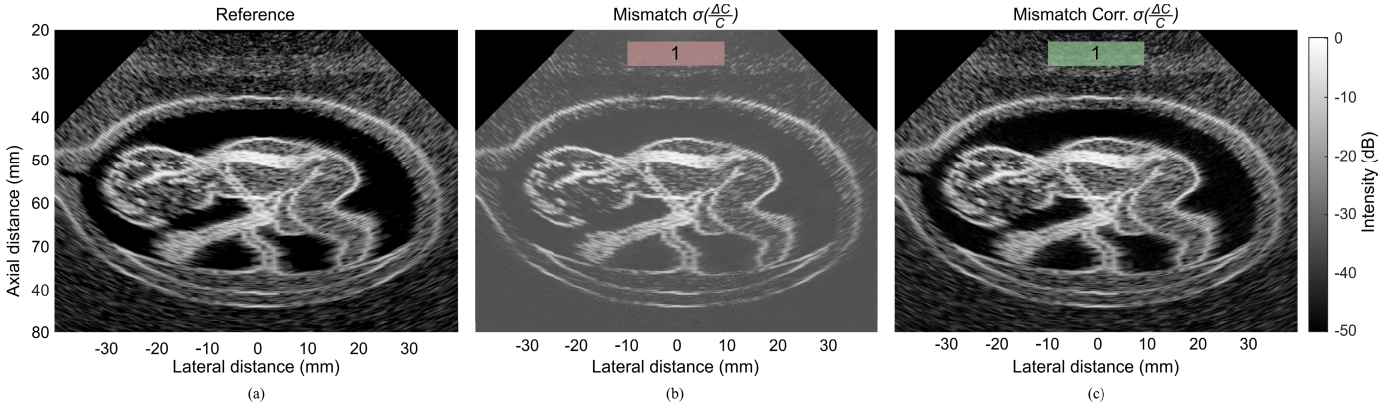

Fig. 13. B-mode images of a fetus phantom simulated with the phased-array transducer: (a) reference, (b) with $\sigma(\Delta C)/C = 1$ before correction, and (c) with $\sigma(\Delta C)/C = 1$ after correction.

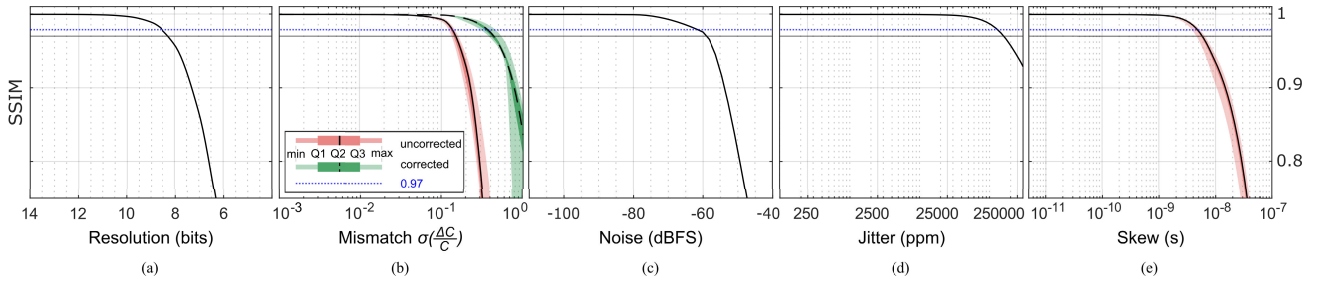

Fig. 14. Interpolated box plot generated from ten MC runs, displaying the SSIM IQM of the B-mode images of the fetus phantom versus (a) resolution, (b) mismatch, (c) noise, (d) jitter, and (e) skew levels for a 12-bit split-unary-CDAC SAR-ADC. The min and max represent the smallest and largest numbers in the dataset, respectively. Q1, Q2, and Q3 are the dataset's first, second, and third quartiles, respectively.

E. Summary

The imaging results of the 128-element phased-array transducer reveal that the two imaging modes lead to different ADC requirements, as shown in Table II, in which the B-mode and color-Doppler requirements were derived from an SSIM value of 0.97, indicating minimal image degradation levels. In addition, it confirms that the requirements depend on the simulated phantom. The fetus phantom leads to more demanding ADC requirements because neighboring anechoic and hyperechoic regions are absent in the cyst phantom. The noise requirements, in particular, are significantly more stringent for the fetus phantom than the cyst phantom. Finally, if the application only targets B-mode imaging, a 9-bit ADC should suffice. However, if the application also requires color-Doppler imaging, a 12-bit ADC would be required. In that case, designing a single ADC that meets both the requirements and can switch to a lower-power mode for B-mode imaging might be an efficient solution.

V. Discussion

A simulation framework was created to quantitatively evaluate the impact of SAR-ADC nonidealities on B-mode and color-Doppler image quality.

A. Design Methodology

Compared with a regular design methodology focused on electrical signal quality, the approach focused on image quality could lead to more area- and power-efficient ultrasound ADCs. First, the results show that capacitor matching requirements

TABLE II
ADC REQUIREMENTS FOR B-MODE (8-BIT ADC AND 12-BIT ADC) AND COLOR-DOPPLER IMAGING BASED ON THE IQMS FOR A 128-ELEMENT PHASED-ARRAY TRANSDUCER

Parameter	Cyst (8b)	Cyst (12b)	Fetus (12b)	Vessel (12b)	Unit
Resolution	8	12	9	12	bits
Mismatch	0.05	0.12	0.15	0.16	$\sigma(\Delta C)/C$
Mismatch corr.	0.15	0.59	0.44	0.23	$\sigma(\Delta C)/C$
Noise	-51.8	-49.4	-59.0	-75.2	dBFS
Jitter	$88 \cdot 10^3$	$121 \cdot 10^3$	$159 \cdot 10^3$	$50 \cdot 10^3$	ppm
Skew	3.4	3.7	5.8	25.0	ns

TABLE III
NUMBER OF REQUIRED CAPACITORS AND SWITCHES FOR THE 12-BIT CONVENTIONAL AND SPLIT-CDAC STRUCTURES USING A UNARY/BINARY SWITCHING SCHEME

CDAC Type	Switching Scheme	Capacitors	Switches
Conventional	Unary	4096	4096
Conventional	Binary	4096	12
Split	Unary	128+1	128
Split	Binary	128+1	12

can be severely relaxed for the design of ultrasound ADCs as long as the transfer function is monotonously increasing. For the targeted 12-bit ADC, this enables the use of the split CDAC architecture, which reduces the number of required capacitors and switches from 4096 to $128 + 1$ (Table III).

Second, calibration can be used to further relax the CDAC matching requirements, enabling the use of smaller capacitors. At some point, however, reducing the capacitor size will negatively affect the thermal noise associated with the CDAC.

Finally, the ADC operation can be adjusted to the required imaging modality. The ADC could operate in the 9-bit mode for B-mode imaging to reduce power consumption, whereas the ADC should operate in the 12-bit mode to capture the smaller signal required for color-Doppler imaging.

B. Image Quality Metrics

The SSIM and CNR metrics match well with human perception for the evaluated cyst phantom and have a clear crossover point at the start of visual image degradation.

The PSNR remains constant until the nonidealities reach the single-channel SQNR level, after which it degrades with a constant slope. This crossover point is not affected by the number of transducer elements but is determined by the single-channel ADC resolution. The crossover point, however, can occur far before any visual degradation in the image becomes visible. Nevertheless, we can observe that for PSNR values above 40 dB, the visual image quality remains high.

In addition, we have observed a dependency of the PSNR on the image contents and chosen DR. In contrast to conventional image sensors, ultrasound data are log-compressed before image reconstruction, resulting in higher PSNRs for hyperechoic regions compared with regions of lower reflectivity. By limiting the image's DR to 50 dB, the PSNR in anechoic regions is artificially increased since the noise below the −50-dBFS limit is filtered out. To a somewhat lesser extent, this is also true for the other IQMs, as the B-mode of the cyst phantom leads to different requirements than the B-mode of the fetus phantom.

The SSIM and RMSE metrics used to evaluate the vessel-phantom have similar crossover points at the start of visual image degradation, indicating that the ADC requirements for an accurate blood flow velocity are similar to those required for a high-quality image.

C. Imaging Modality-Dependent Resolution

The ADC resolution requirements are derived from the DR of the signals required to generate the images. Assuming perfect TGC, increasing the ADC resolution beyond this range is ineffective. A 12-bit ADC was required to capture the smaller reflections induced by blood, whereas only 8- and 9-bit ADCs were required to generate the B-mode images of the cyst and fetus phantoms, respectively. Note that if the TGC requirements were to be relaxed, the ADC resolution would need to be increased.

It is important to note that the results presented in this study are restricted to fundamental imaging modes and cannot directly be extrapolated to harmonic imaging modes, such as contrast-enhanced ultrasound (CEUS) and super-resolution imaging (SRU). Depending on the medium and the transmission pulse type, tissue harmonics are between 6 and 30 dB weaker than fundamental echoes [34]. It should, therefore, be expected that a similar increase in ADC resolution will be needed to capture these echoes. Moreover, more stringent linearity requirements should be expected to ensure that ADC-induced harmonics are well below the tissue harmonics. A quantitative simulation study of these effects is future work.

D. Transducer Topology

It is not trivial to translate the obtained ADC requirements for the 128-element phased array to other array configurations since there is no linear relationship between the electrical parameters and the perceived image quality. Nevertheless, some recommendations can be made on this topic. First, increasing the number of transducer elements leads to a higher PSNR for all the introduced nonidealities due to the coherent summation of RF data. However, this effect is limited by the opening angles, as distant transducer elements do not receive coherent information for all the scanlines. It is similar to linear arrays, where only a subset of the transducer elements are used to generate a single scanline.

The applicability of these results for 2-D arrays with integrated electronics and the effect of nonidealities in combination with subaperture beamforming [35], [36] on the image quality requires further study. The results will likely depend on the subaperture size and the location of the ADC in the signal chain (before/after beamforming).

Finally, the physical transducer element size also affects ADC requirements. Larger elements have a higher DR, leading to more demanding ADC requirements. Furthermore, in the case of an identical aperture with increased element sizes, the reduced number of elements leads to more demanding matching requirements.

E. Transducer Frequency

The chosen transducer frequency will impact some of the ADC requirements. For example, increasing the transducer frequency will result in more stringent jitter and skew specs. However, the noise, resolution, and mismatch requirements will likely remain the same. In addition, a higher sampling rate and increased bandwidth will lead to technology- and implementation-dependent increases in area and power consumption [12].

F. Evaluation Method

The environment was well-controlled by performing a numerical simulation study, making the resulting data well-suited for comparison. The effect that individual nonidealities have on the image has been investigated. For future simulations, it would be interesting to see how the image quality and correction operation are affected when multiple nonidealities are applied concurrently or when the applied nonidealities are correlated (e.g., power supply noise). Furthermore, it would be interesting to see how the studied nonidealities affect new imaging modalities such as CEUS and SRU. In addition, other nonidealities, such as substrate and channel-crosstalk and charge injection, may be investigated in future studies.

VI. Conclusion

In this study, we have investigated how the area and power consumption of SAR-ADCs can be reduced without negatively affecting the B-mode and color-Doppler image quality of phased-array ultrasound transducers. We performed a simulation study in which RF data were acquired with a 128-element phased-array transducer in Field II. The RF data were entered into an ideal and nonideal SAR-ADC simulation model. Several nonidealities were applied to the most common SAR-ADC architectures. B-mode and color-Doppler images were reconstructed and compared against those generated from the ideal ADC's output.

We found that B-mode imaging and color-Doppler imaging are inherently resilient against capacitor mismatch, enabling the use of the area- and power-efficient split-CDAC structure. Compared with the conventional 12-bit (low-mismatch) unary CDAC, the split-CDAC structure requires only 3% of the capacitors and switches while consuming only 3% of the switching power consumption. Correcting the transfer curve of the ADC by subtracting the INL further increases the robustness to capacitor mismatch to 59% for B-mode imaging and 23% for color-Doppler imaging, enabling the use of smaller capacitors and possibly leading to an even smaller area and lower power consumption. Ultimately, the presented strategy can be used to design more area- and power-efficient ADCs for handheld and wearable ultrasound devices and other ultrasound devices using in-probe digitization.

References

[1] C. F. Dietrich, C. B. Sirlin, M. O'Boyle, Y. Dong, and C. Jenssen, "Editorial on the current role of ultrasound," *Appl. Sci.*, vol. 9, no. 17, p. 3512, Aug. 2019. [Online]. Available: https://www.mdpi.com/2076-3417/9/17/3512

[2] D. P. Frush, M. J. Callahan, B. D. Coley, H. R. Nadel, and R. P. Guillerman, "Comparison of the different imaging modalities used to image pediatric oncology patients: A COG diagnostic imaging committee/SPR oncology committee white paper," *Pediatric Blood Cancer*, vol. 70, no. S4, p. 30298, Jun. 2023.

[3] Y. Baribeau et al., "Handheld point-of-care ultrasound probes: The new generation of POCUS," *J. Cardiothoracic Vascular Anesthesia*, vol. 34, no. 11, pp. 3139–3145, Nov. 2020. [Online]. Available: https://www.sciencedirect.com/science/article/pii/S1053077020306340

[4] H. Huang, R. S. Wu, M. Lin, and S. Xu, "Emerging wearable ultrasound technology," *IEEE Trans. Ultrason., Ferroelectr., Freq. Control*, vol. 71, no. 7, pp. 713–729, Jul. 2024.

[5] H. Hu et al., "A wearable cardiac ultrasound imager," *Nature*, vol. 613, no. 7945, pp. 667–675, Jan. 2023.

[6] M. Lin et al., "A fully integrated wearable ultrasound system to monitor deep tissues in moving subjects," *Nature Biotechnol.*, vol. 42, no. 3, pp. 448–457, Mar. 2024.

[7] M.-C. Chen et al., "A pixel pitch-matched ultrasound receiver for 3-D photoacoustic imaging with integrated delta-sigma beamformer in 28-nm UTBB FD-SOI," *IEEE J. Solid-State Circuits*, vol. 52, no. 11, pp. 2843–2856, Nov. 2017.

[8] C. Chen et al., "A pitch-matched front-end ASIC with integrated subarray beamforming ADC for miniature 3-D ultrasound probes," *IEEE J. Solid-State Circuits*, vol. 53, no. 11, pp. 3050–3064, Nov. 2018.

[9] J. M. Rothberg et al., "Ultrasound-on-chip platform for medical imaging, analysis, and collective intelligence," *Proc. Nat. Acad. Sci. USA*, vol. 118, no. 27, Jul. 2021, Art. no. 2019339118. [Online]. Available: https://github.com/bmurmann/ADC-survey/blob/main/xls/ADCsurvey_rev20231003.xlsx

[10] P. Guo et al., "A pitch-matched transceiver ASIC for 3D ultrasonography with micro-beamforming ADCs based on passive boxcar integration and a multi-level datalink," in *Proc. IEEE Symp. VLSI Technol. Circuits (VLSI Technol. Circuits)*, Jun. 2023, pp. 1–2.

[11] D. Duncker et al., "Reprocessing of electrophysiology material in EHRA countries: An EHRA young EP survey," *EP Europace*, vol. 23, no. 3, pp. 479–485, Mar. 2021, doi: 10.1093/europace/euaa250.

[12] B. Murmann. *ADC Performance Survey 1997–2023*. [Online]. Available: https://github.com/bmurmann/ADC-survey

[13] A. Carovac, F. Smajlovic, and D. Junuzovic, "Application of ultrasound in medicine," *Acta Inf. Medica*, vol. 19, no. 3, pp. 71–168, 2011.

[14] Y. M. Hopf et al., "A pitch-matched transceiver ASIC with shared hybrid beamforming ADC for high-frame-rate 3-D intracardiac echocardiography," *IEEE J. Solid-State Circuits*, vol. 57, no. 11, pp. 3228–3242, Nov. 2022.

[15] J. Lee et al., "A 36-channel auto-calibrated front-end ASIC for a pMUT-based miniaturized 3-D ultrasound system," *IEEE J. Solid-State Circuits*, vol. 56, no. 6, pp. 1910–1923, Jun. 2021.

[16] T. Kim, S. Shin, and S. Kim, "An 80.2 dB DR 23.25 mW/channel 8-channel ultrasound receiver with a beamforming embedded SAR ADC," *IEEE Trans. Circuits Syst. II, Exp. Briefs*, vol. 66, no. 9, pp. 1487–1491, Sep. 2019.

[17] Z. Chen et al., "Impact of bit errors in digitized RF data on ultrasound image quality," *IEEE Trans. Ultrason., Ferroelectr., Freq. Control*, vol. 67, no. 1, pp. 13–24, Jan. 2020.

[18] J. L. McCreary and P. R. Gray, "All-MOS charge redistribution analog-to-digital conversion techniques. I," *IEEE J. Solid-State Circuits*, vol. SSC-10, no. 6, pp. 371–379, Dec. 1975.

[19] M. Pelgrom, "Digital-to-analog conversion," in *Analog-to-Digital Conversion*, 4th ed., Cham, Switzerland: Springer, 2017, pp. 203–283.

[20] M. Saberi, R. Lotfi, K. Mafinezhad, and W. A. Serdijn, "Analysis of power consumption and linearity in capacitive digital-to-analog converters used in successive approximation ADCs," *IEEE Trans. Circuits Syst. I, Reg. Papers*, vol. 58, no. 8, pp. 1736–1748, Aug. 2011.

[21] W. R. Bennett, "Spectra of quantized signals," *Bell Syst. Tech. J.*, vol. 27, no. 3, pp. 446–472, Jul. 1948.

[22] B. Razavi, "Noise," in *Design of Analog CMOS Integrated Circuits*, 2nd ed., New York, NY, USA: McGraw-Hill, 2017, ch. 7, pp. 228–236.

[23] J. A. Jensen, "Field: A program for simulating ultrasound systems," *Med. Biol. Eng. Comput.*, vol. 34, no. 1, pp. 351–352, Jan. 1996.

[24] J. Jensen and N. Svendsen, "Calculation of pressure fields from arbitrarily shaped, apodized, and excited ultrasound transducers," *IEEE Trans. Ultrason., Ferroelectr., Freq. Control*, vol. 39, no. 2, pp. 262–267, Feb. 1992.

[25] J. A. Jensen and P. Munk, *Computer Phantoms for Simulating Ultrasound B-Mode CFM Images*. Boston, MA, USA: Springer, 1997, pp. 75–80, doi: 10.1007/978-1-4419-8588-0_12.
[26] P. J. Brands, A. P. G. Hoeks, L. Hofstra, and R. S. Reneman, "A noninvasive method to estimate wall shear rate using ultrasound," *Ultrasound Med. Biol.*, vol. 21, no. 2, pp. 171–185, Jan. 1995.
[27] D. Zander et al., "Ultrasound image optimization ('knobology): B-mode," *Ultrasound Int. Open*, vol. 6, no. 1, pp. E14–E24, Aug. 2020.
[28] C. Kasai, K. Namekawa, A. Koyano, and R. Omoto, "Real-time two-dimensional blood flow imaging using an autocorrelation technique," *IEEE Trans. Sonics Ultrason.*, vol. SU-32, no. 3, pp. 458–464, May 1985.
[29] C. Dietrich et al., "General principles of image optimization in EUS," *Endoscopic Ultrasound*, vol. 10, no. 3, p. 168, 2021.
[30] R. Dosselmann and X. Dong Yang, "Existing and emerging image quality metrics," in *Proc. Can. Conf. Electr. Comput. Eng.*, 2005, pp. 1906–1913.
[31] W. Zhou, A. C. Bovik, H. R. Sheikh, and E. P. Simoncelli, "Image quality assessment: From error visibility to structural similarity," *IEEE Trans. Image Process.*, vol. 13, pp. 600–612, 2004.
[32] M. Patterson, "The improvement and quantitative assessment of B-mode images produced by an annular array/cone hybrid," *Ultrason. Imag.*, vol. 5, no. 3, pp. 195–213, Jul. 1983.
[33] A. Rodriguez-Molares, O. M. H. Rindal, J. D'Hooge, S. Måsøy, A. Austeng, and H. Torp, "The generalized contrast-to-noise ratio," in *Proc. IEEE Int. Ultrason. Symp. (IUS)*, Oct. 2018, pp. 1–4.
[34] F. Guidi, L. Demi, and P. Tortoli, "Experimental and simulation study of harmonic components generated by plane and focused waves," *Ultrasonics*, vol. 116, Sep. 2021, Art. no. 106504. [Online]. Available: https://www.sciencedirect.com/science/article/pii/S0041624X21001347
[35] G. R. Lockwood, J. R. Talman, and S. S. Brunke, "Real-time 3-D ultrasound imaging using sparse synthetic aperture beamforming," *IEEE Trans. Ultrason., Ferroelectr., Freq. Control*, vol. 45, no. 4, pp. 980–988, Jul. 1998.
[36] J. A. Jensen et al., "Ultrasound research scanner for real-time synthetic aperture data acquisition," *IEEE Trans. Ultrason., Ferroelectr., Freq. Control*, vol. 52, no. 5, pp. 881–891, May 2005.

Nikola Radeljic-Jakic (Graduate Student Member, IEEE) received the B.Sc. and M.Sc. degrees in electrical engineering from Delft University of Technology, Delft, The Netherlands, in 2013 and 2015, respectively, where he is currently pursuing the Ph.D. degree with the Electronic Instrumentation Laboratory.

In 2016, he joined Oldelft Ultrasound, Delft, where he is currently working as an ASIC Designer for ICE catheters and TEE probes. His main research field is the integrated circuit design for digital 3-D-ICE probes.

Adriaan J. Flikweert (Member, IEEE) received the M.Sc. and Ph.D. degrees in applied physics from Eindhoven University of Technology, Eindhoven, The Netherlands, in 2004 and 2008, respectively.

For his master's thesis, he was with Akzo Nobel, Arnhem, The Netherlands, where he was a part of the research team for flexible solar cells. As part of his Ph.D. project, he had a traineeship at the Space Plasmas and Plasma Propulsion Group, Australian National University, Canberra, ACT, Australia. From 2008 to 2012, he was with Forschungszentrum Jülich, Jülich, Germany, where he was a Researcher at the Photovoltaics Department. From 2012 to 2014, he was at the Research and Development Department, Applus RTD, Rotterdam, The Netherlands. In 2014, he joined Oldelft Ultrasound, Delft, The Netherlands, as an Acoustic Engineer developing ultrasound transducers. He has authored and co-authored more than 30 technical papers.

Nuriel N. M. Rozsa (Member, IEEE) received the B.Sc. degree (cum laude) and M.Sc. degree (honors program certificate) in electrical engineering from Delft University of Technology, Delft, The Netherlands, in 2018 and 2021, respectively, where he is currently pursuing the Ph.D. degree with the Electronic Instrumentation Laboratory, working within the Ultra-X-Treme Research Program on high frame-rate 3-D ultrasound imaging probes for imaging the abdominal aorta.

Hendrik J. Vos (Member, IEEE) received the M.Sc. degree in applied physics from Delft University of Technology, Delft, The Netherlands, in 2004, and the Ph.D. degree from the Department of Biomedical Engineering, Erasmus University Medical Center, Rotterdam, The Netherlands, in 2010.

He worked as a Postmaster Researcher with the University of Florence, Florence, Italy, and a Contract Researcher for the petrochemical industry on cutting-edge ultrasonic solutions. He is currently an Associate Professor with the Erasmus University Medical Center, and Delft University of Technology, Delft. He received a Dutch NWO-TTW-VIDI personal grant in 2018. His research interests include acoustical array technology for biomedical imaging in all its aspects: transducers, 2-D and 3-D beamforming, cardiac shear waves, ultrafast Doppler, contrast imaging, and related subclinical and clinical studies.

Michiel A. P. Pertijs (Senior Member, IEEE) received the M.Sc. and Ph.D. degrees (cum laude) in electrical engineering from Delft University of Technology, Delft, The Netherlands, in 2000 and 2005, respectively.

From 2005 to 2008, he was with the National Semiconductor, Delft, where he designed precision operational amplifiers and instrumentation amplifiers. From 2008 to 2009, he was a Senior Researcher with imec/Holst Centre, Eindhoven, The Netherlands. In 2009, he joined the Electronic Instrumentation Laboratory, Delft University of Technology, where he is now an Associate Professor. He heads a research group focusing on integrated circuits for ultrasound applications. In 2024, he co-founded the company SonoSilicon, Delft, and Hangzhou, China, which specializes in chip technology for next-generation medical ultrasound devices. He has authored or co-authored two books, four book chapters, 15 patents, and more than 170 technical papers.

Dr. Pertijs is a member of the technical program committees of the European Solid-State Circuits Conference (ESSCIRC), the IEEE International Ultrasonics Symposium (IUS), and the International Solid-State Circuits Conference (ISSCC). He received the ISSCC 2005 Jack Kilby Award and the JSSC 2005 Best Paper Award. For his Ph.D. research on high-accuracy CMOS smart temperature sensors, he received the 2006 Simon Stevin Gezel Award from the Dutch Technology Foundation STW. In 2014 and 2023, he was elected as a Best Teacher of the EE Program at Delft University of Technology. He served as an Associate Editor (AE) for IEEE OPEN JOURNAL OF SOLID-STATE CIRCUITS (O-JSSC) and IEEE JOURNAL OF SOLID-STATE CIRCUITS (JSSC).